Supplementary Information

A Highly Efficient Diatomic Nickel Electrocatalyst for CO_2 reduction

Meng-Jiao Sun,[a,b] Zhi-Wei Gong,[a,b] Jun-Dong Yi,[b] Teng Zhang,[b,c]* Xiaodong Chen,[d] Rong Cao[b,c]*

[a] College of Chemistry, Fuzhou University, Fuzhou, 350108, China

[b] State Key Laboratory of Structural Chemistry, Fujian Institute of Research on the Structure of Matter, Chinese Academy of Sciences, Fuzhou, Fujian, 350002, China

[c] University of the Chinese Academy of Sciences, Beijing, 100049, China

[d] Innovative Centre for Flexible Devices, School of Materials Science and Engineering, Nanyang Technological University, 50 Nanyang Avenue, Singapore 639798, Singapore

1. Experimental Details

General Information. All chemicals were used as received without purification except for aniline. Aniline was purified through redistillation. Powder X-ray diffraction (PXRD) patterns were recorded on a Miniflex 600 diffractometer using Cu Kα radiation (λ = 0.154 nm). Thermogravimetric analyses (TGA) were performed under a nitrogen atmosphere by using an SDT Q600 thermogravimetric analyser. The contents of C, H, and N were record by Elemental analyses (EA) on an Elementar Vario EL III analyzer. Inductively Coupled Plasma Optical Emission spectrometer (ICP-OES) measurements detected the content of Ni in samples. The Infrared spectroscopy (IR) with attenuated total reflection was tested on a Bruker VERTEX70 over a range of 400 - 4000 cm^{-1}. X-ray photoelectron spectroscopy (XPS) measurements were performed on an ESCALAB 250Xi X-ray photoelectron spectrometer (Thermo Fisher) using an Al Kα source (15 kV, 10 mA). N2 adsorption-desorption isotherm and the Brunauer-Emmett-Teller (BET) surface area measurements were measured using Micromeritics ASAP 2460 instrument. CO2 adsorption-desorption isotherms were measured by using Micrometrics ASAP 2020 instrument. Field Emission Scanning Electron Microscope (FESEM) images were performed on JSM6700-F (JEOL) SEM. Transmission electron microscope (TEM) images were recorded by a FEIT 20 working at 200 kV. Aberration-corrected High-angle annular dark-field scanning transmission electron microscopy (HAADF-STEM) images and the EDS of samples were performed with a Titan Cubed Themis G2 300 (FEI) high-resolution transmission electron microscope operated at 200 kV. The Ni L-edge NEXAFS measurements were carried out at the BL12b bending magnet beamline in the National Synchrotron Radiation Laboratory (NSRL) in a total electron yield (TEY) mode by collecting the sample drain current. The base pressure of the UHV chamber was better than 5 × 10-8 Pa. The synchrotron beam was monochromatized via a varied line-spacing plane grating and refocused by a toroidal mirror. X-ray absorption fine structure (XAFS) measurment and data analysis: XAFS spectra at the Ni K-edge (8332 eV) was collected at BL14W1 station in Shanghai Synchrotron Radiation Facility (SSRF). The Ni K-edge X-ray absorption near edge structure (XANES) data were recorded in a transmission mode. The gas products were quantified by gas chromatograph (GC) (Agilent 7890A). The liquid products were quantified by nuclear magnetic resonance (NMR) (JEOL ECZ400S) spectroscopy using dimethyl sulfoxide as an internal standard.

Synthesis of Ni-PANI@C's and Ni-N@C's. In a typical procedure, 0.4 g ketjen black was dispersed with 50 mL of 1 M HCl solution under ultrasonication for 15 min. Aniline, $NiCl_2 \cdot 6H_2O$ and $(NH_4)_2S_2O_8$ were then added subsequently to the suspension under stirring and allowed to react at 5 °C for 24 h. After the reaction, the solid was centrifuged and dried under vacuum as Ni-PANI@C precursors, then subject to 1000 °C pyrolysis (N_2 atmosphere, ramp rate 5 °C/min) for one hour. After pyrolysis, the solid was stirred in 0.1 M HCl to remove residual salt and metal nanoparticles, filtered, washed with deionized water, and dried under vacuum to afford Ni-N@C catalysts. Catalysts with different Ni and N loadings were obtained by altering the feed ratio of aniline, nickel chloride in the first step (Table S1).

Table S1. The synthesis conditions and elemental analysis results of Ni-N@C materials.

Materials	Ketjen black (g)	Aniline (mL)	APS (g)	$NiCl_2 \cdot 6H_2O$ (mg)	Ni wt%	N wt%
Ni-N@C0	0.4	2	0	250	0.055	0.36
Ni-N@C1	0.4	0.5	1.25	250	0.237	2.40
Ni-N@C2	0.4	1	2.5	250	0.199	2.81
Ni-N@C4	0.4	2	5	250	0.085	3.20
N@C	0.4	0.5	1.25	0	N/A	2.33
Ni-N@C1-1%	0.4	0.5	1.25	1000	1.067	2.85

Preparation of Working Electrode. In a typical procedure, 5 mg of Ni-N@C catalysts, and 40 μL of 5 wt% Nafion solution (in ethanol/water) were dispersed in 1 mL of isopropanol to form a homogeneous ink by 90 min of ultrasonication. Sixty microliters of the prepared ink were loaded onto the two sides of a carbon paper electrode (TGP-H-090, 1×1 cm^2).

Electrochemical Measurements. Electrochemical experiments were carried out in a gas-tight H-cell with cathodic and anodic compartments separated by proton exchange membrane (Nafion-117). Each compartment contained 60 mL of 0.5 M $KHCO_3$ aqueous solution. A CO_2 flow of 30 sccm was applied continuously to achieve a CO_2-saturated solution (pH=7.2). A Pt gauze was used as counter electrode and an Ag/AgCl/KCl (sat'd) electrode (0.197 V vs. SHE) was used as reference electrode. All potentials reported were converted to the RHE reference scale.

GC detection of gas products. CO_2 reduction was conducted under the potentiostatic mode at each potential for 30 min. 1 mL of gas phase product was injected into the gas-sampling loop of gas chromatograph (GC) at 15 min of electrolysis. The H_2 and CO products were quantified by a thermal conductivity detector (TCD) and flame ionization detector (FID) of GC, respectively. For long-term electrolysis, the outlet gas was sampled every 30 min for CO and H_2 quantification. The electrochemical impedance spectroscopy (EIS) was performed at −1.65 V (vs. Ag/AgCl) in 0.2 M Na_2SO_4 aqueous solution with an IM6ex (Zahner, Germany) potentiostat.

The faradaic efficiency (FE) and turnover frequency (TOF) for CO production are calculated as follow:

$$FE = \frac{J_{CO}}{J_{total}} = \frac{v_{CO} \times N \times F}{J_{total}}$$

J_{CO} : partial current density for CO production;

J_{total}: total current density;

N: the number of electron transferred for product formation, which is 2 for CO;

v_{CO}: the production rate of CO (measured by GC);

F: Faradaic constant, 96485 C mol^{-1};

$$TOF = \frac{I_{product}/NF}{m_{cat} \times \omega/M_{Ni}} \times 3600$$

$I_{product}$: partial current density for CO production, A;

N: the number of electrons transferred for product formation, which is 2 for CO;

F: Faradaic constant, 96485 C mol^{-1};

m_{cat}: catalyst mass in the electrode, g;

ω: Ni loading in the catalyst;

M_{Ni}: atomic mass of Ni, 58.69 g mol^{-1}.

2. Supplementary Figures and Tables

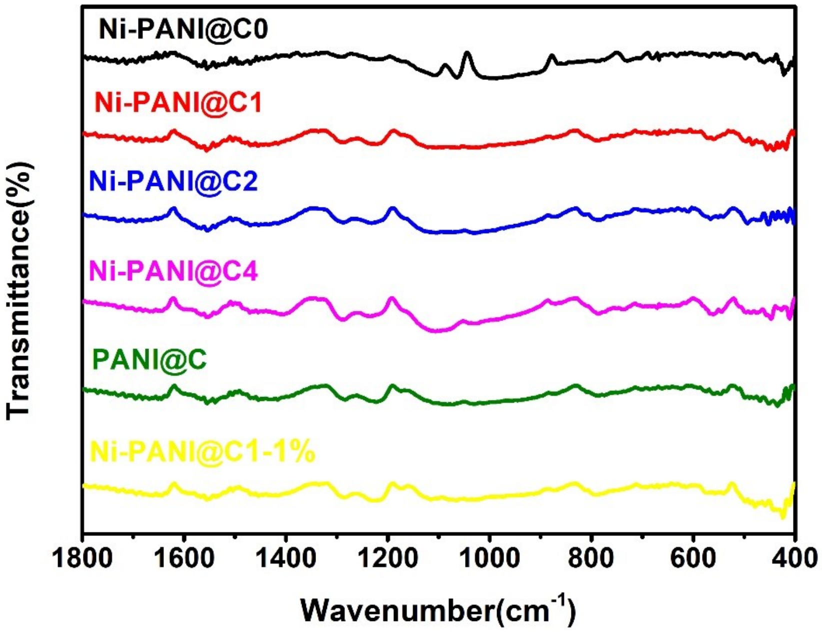

Figure S1. FTIR spectra of Ni-PANI@C precursors.

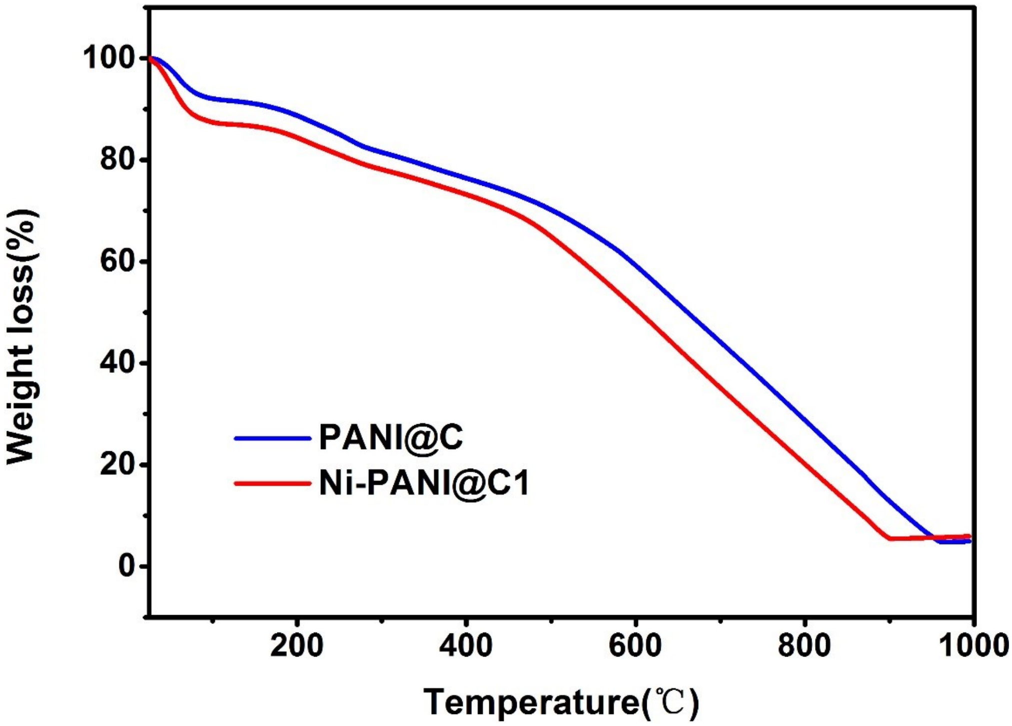

Figure S2. TGA curves of PANI@C and Ni-PANI@C1.

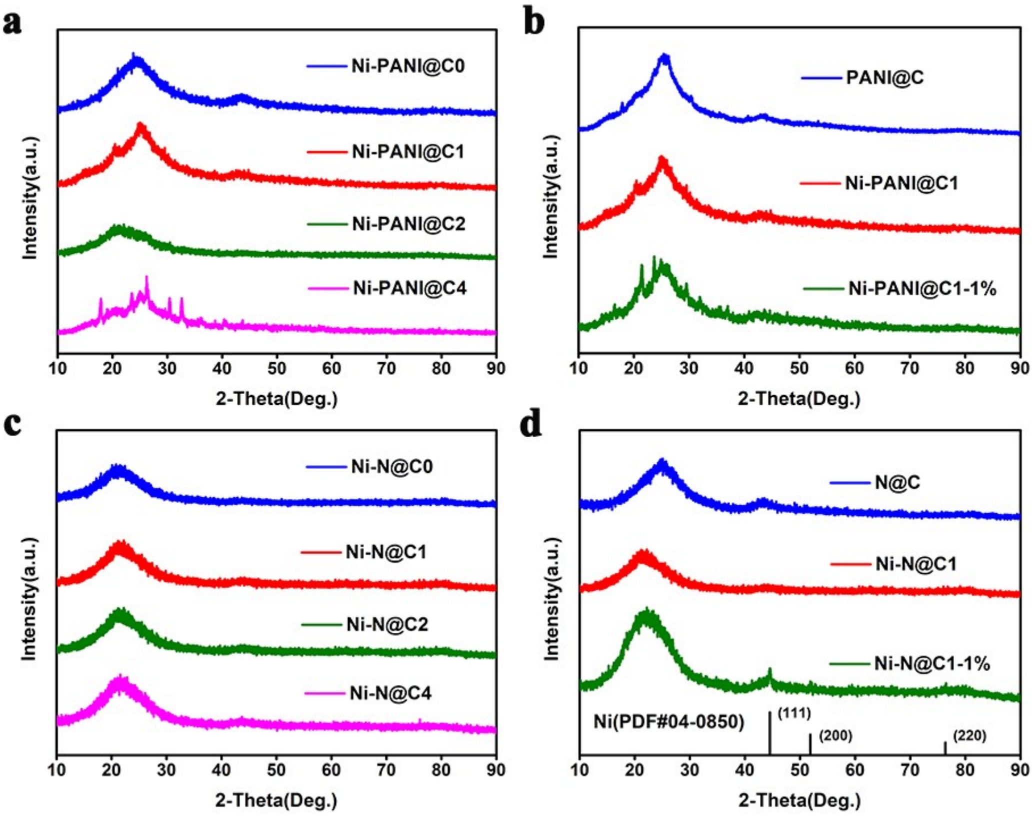

Figure S3. XRD patterns of Ni-PANI@Cs (a, b) and Ni-N@Cs (c, d).

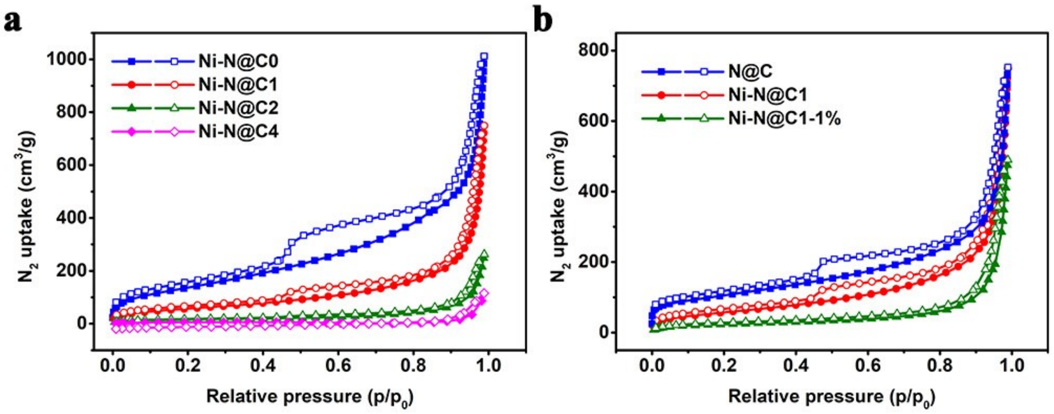

Figure S4. N_2 adsorption and desorption isotherms at 77 K for Ni-N@C catalysts.

Table S2. Porous characteristics of Ni-N@C catalysts.

Sample	**S_{BET} (m^2/g)**
Ni-N@C0	522
Ni-N@C1	215
Ni-N@C2	57
Ni-N@C4	20
N@C	373
Ni-N@C1-1%	85

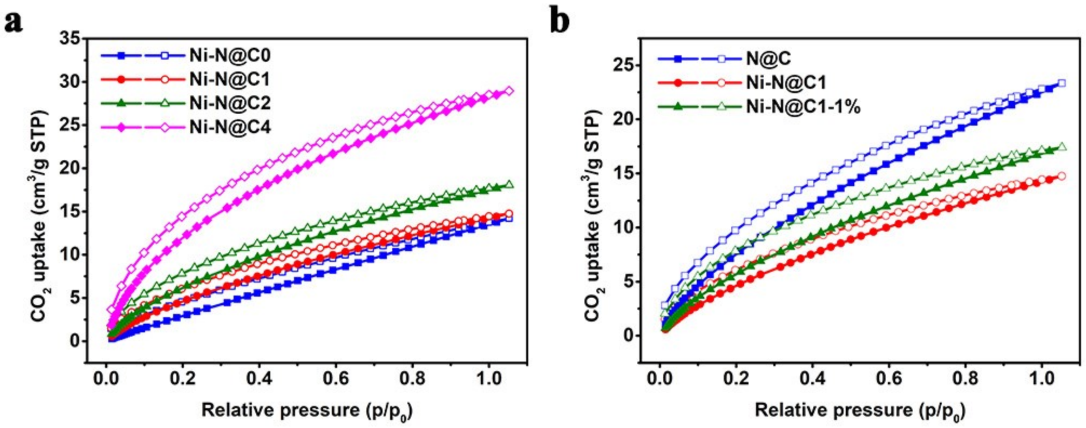

Figure S5. CO_2 adsorption and desorption isotherms at 298 K for Ni-N@C catalysts.

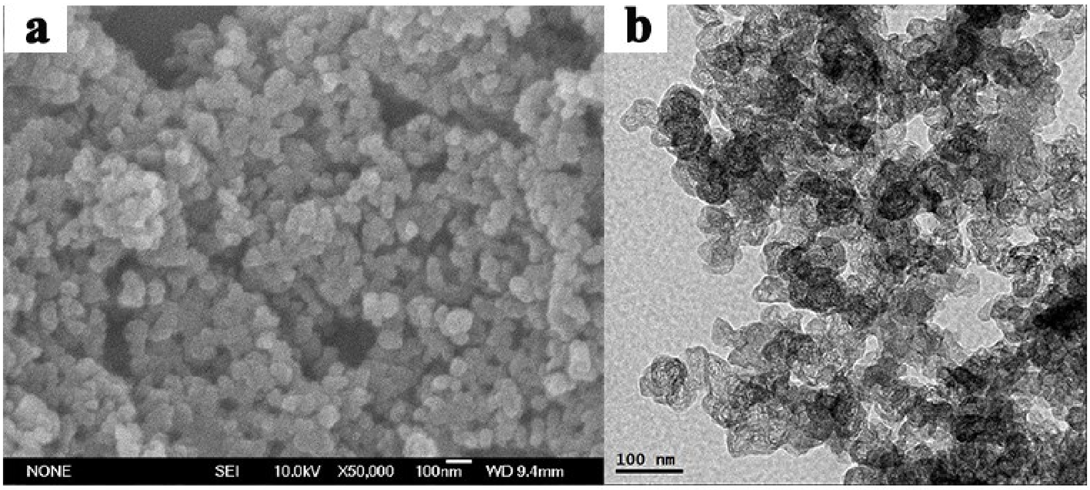

Figure S6. (a) SEM image, (b) TEM image of Ni-N@C1.

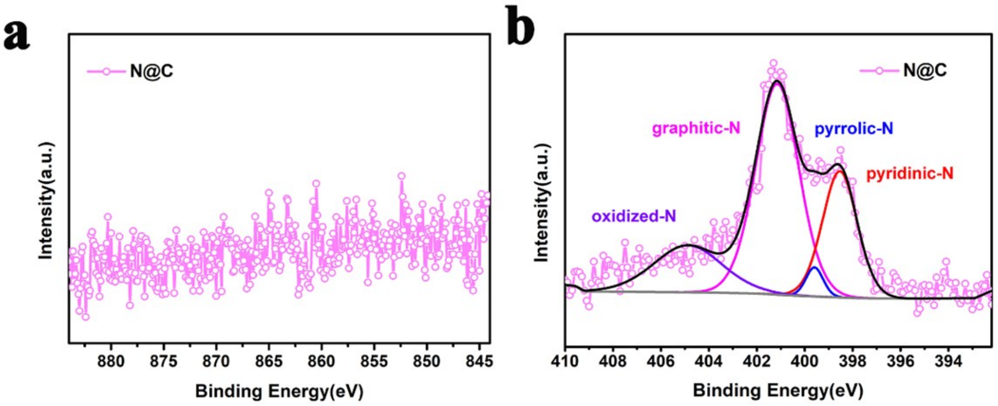

Figure S7. XPS spectra of the Ni 2p region and N 1s region of N@C.

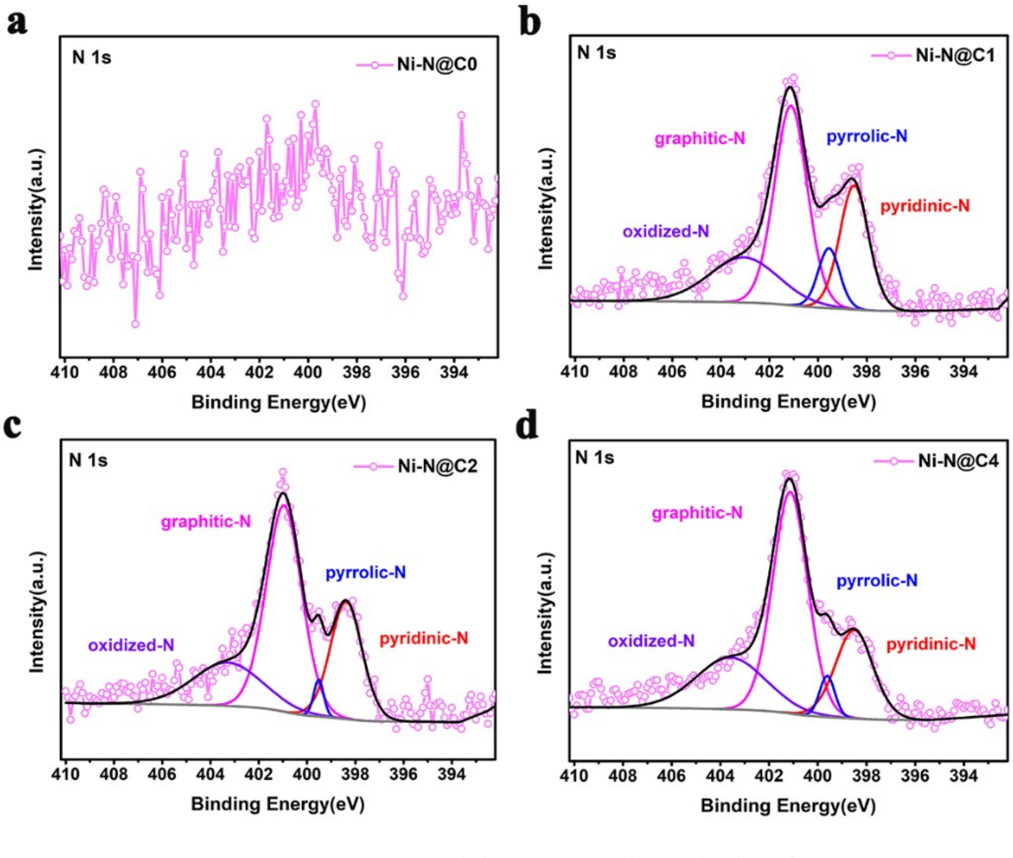

Figure S8. XPS spectra of the N 1s region of Ni-N@C's.

Table S3. The content of different types of nitrogen in Ni-N@Cs based on XPS.

Sample	Graphitic-N (%)	Pyridinic-N (%)	Pyrrolic-N (%)	Oxidized-N (%)
Ni-N@C0	-	-	-	
Ni-N@C1	45.0	25.0	8.75	21.2
Ni-N@C2	50.9	25.5	2.83	20.8
Ni-N@C4	50.3	21.7	4.20	23.8
N@C	52.5	25.4	3.39	18.6

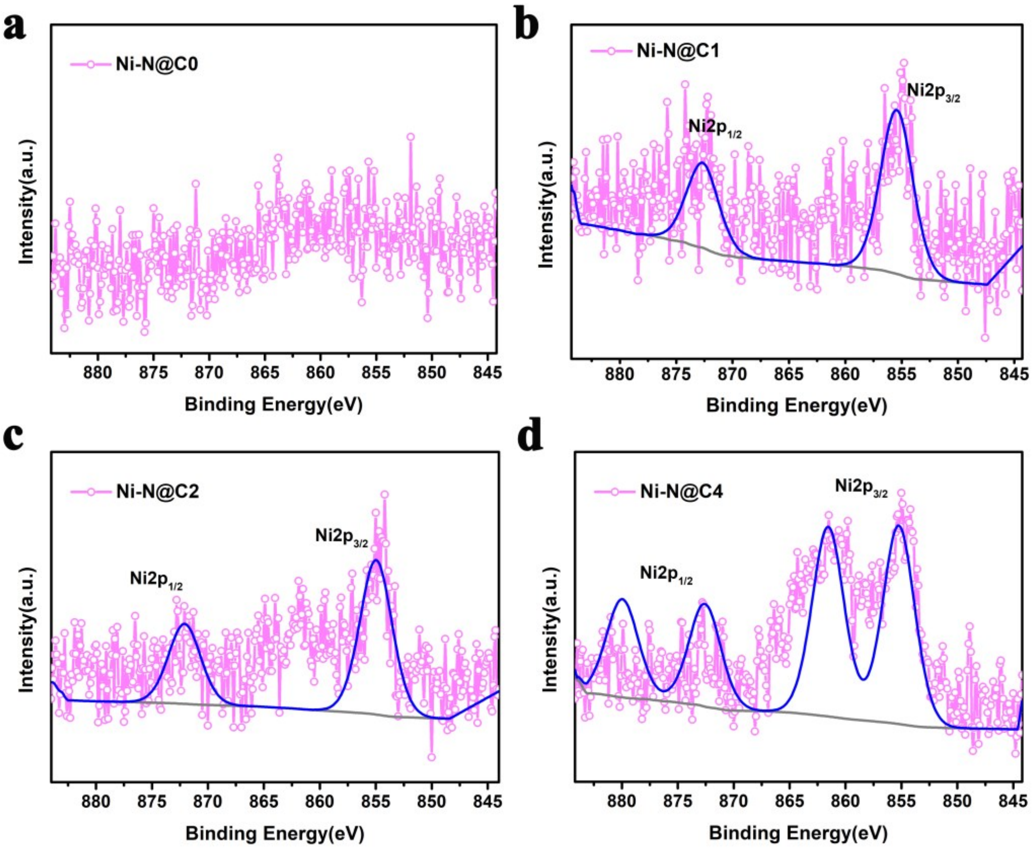

Figure S9. XPS spectra of the Ni 2p region of Ni-N@C's.

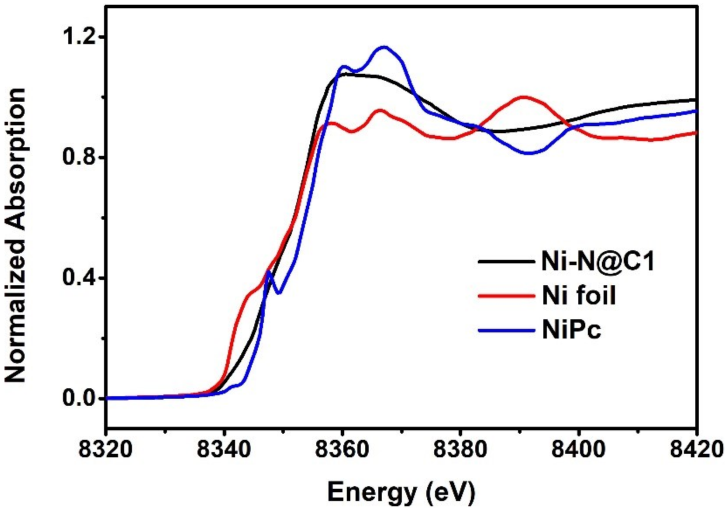

Figure S10. Normalized Ni K-edge XANES spectra of Ni-N@C1 and the corresponding reference samples.

EXAFS fitting of Ni-N@C1. EXAFS fitting was performed using the Artemis program of the IFEFFIT package.[1] Fits were performed with a *k*-weight of 3 in *R*-space, with *k* range 3.000-12.037 Å^{-1} and *R* range 1.0-3.0 Å. As the R-space spectrum of Ni-N@C1 indicates two separate peaks that may correspond to Ni-N and Ni-Ni scattering paths, respectively (Figure S11), paths from two structure models, metallic nickel and nickel(II) phthalocyanine (NiPc), were taken for fitting. Refinement was performed by optimizing an amplitude factor S_0^2 and energy shift ΔE_0 which are common to both paths, in addition to parameters for bond length (ΔR) and Debye-Waller factor (σ^2). An additional parameter (molar fraction of Ni fitting in diatomic environment, x) was introduced to quantify the relative contents of single-atomic NiN_4 and diatomic Ni_2N_6 species. The degeneracy (N) for the two paths were adjusted with respect to x:

$N(\text{Ni-Ni}) = x$

$N(\text{Ni-N}) = 3x+4(1-x) = 4-x$

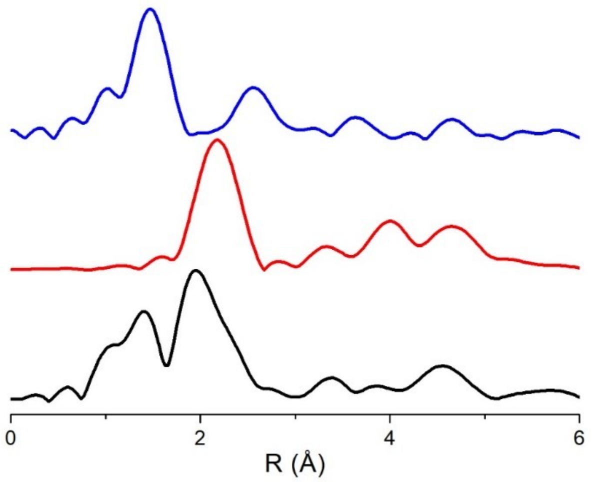

Figure S11. Comparisons of R-space EXAFS spectra of Ni-N@C1 (black) with Ni metal (red) and nickel(II) phthalocyanine (blue).

Table S4. EXAFS fitting results of Ni-N@C1.

Fitting range	k 3.000 – 12.037 Å^{-1}	R (Ni-N) (Å)	1.85±0.02
	R 1.0 – 3.0 Å	σ^2 (Ni-N) (Å^2)	0.0159±0.0051
R-factor	1.90%	R (Ni-Ni) (Å)	2.44±0.01
S_0^2	1.44±0.54	σ^2 (Ni-Ni) (Å^2)	0.0059±0.0016
ΔE_0 (eV)	-19.8±2.8	x	0.73±0.38

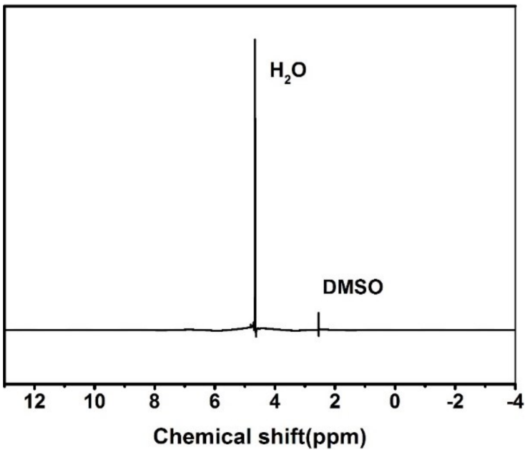

Figure S12. ^{1}H NMR spectra of the electrolyte after CO_2 reduction electrolysis 0.5h at −0.9 V (vs.RHE) for the Ni-N@C1.

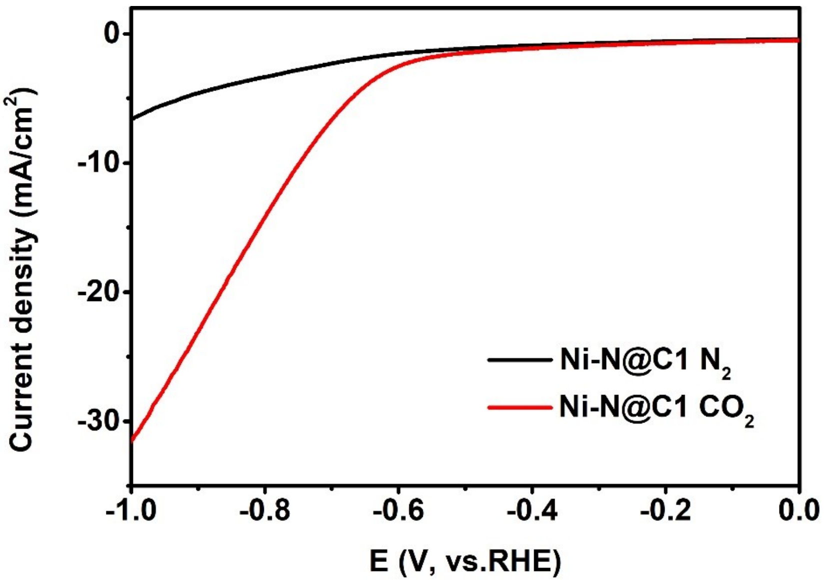

Figure S13. Linear sweep voltammetric curves of Ni-N@C1 in N_2-saturated and CO_2-saturated 0.5 M $KHCO_3$ electrolyte.

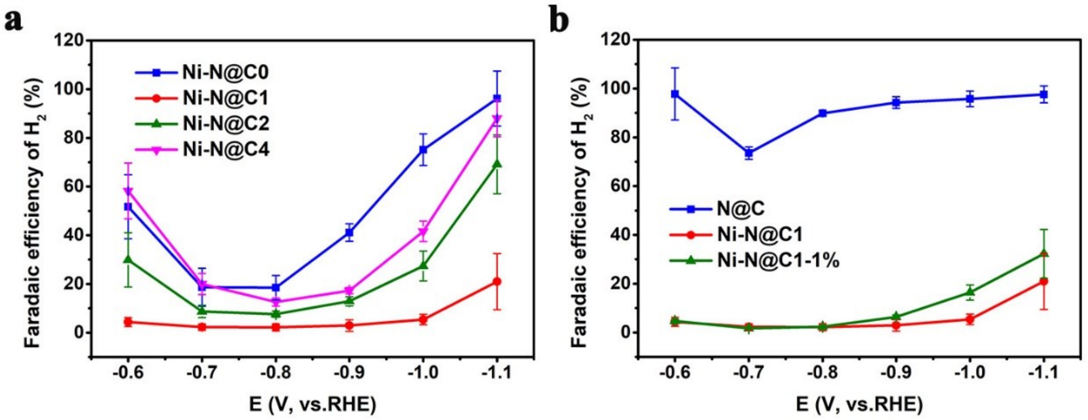

Figure S14. Faradaic efficiencies of H_2.

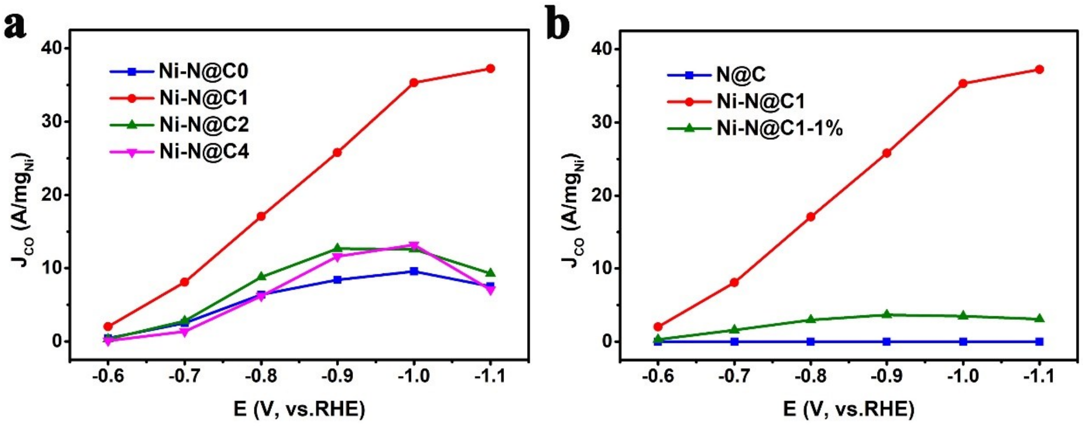

Figure S15. Jco of per milligram Ni for the catalysts.

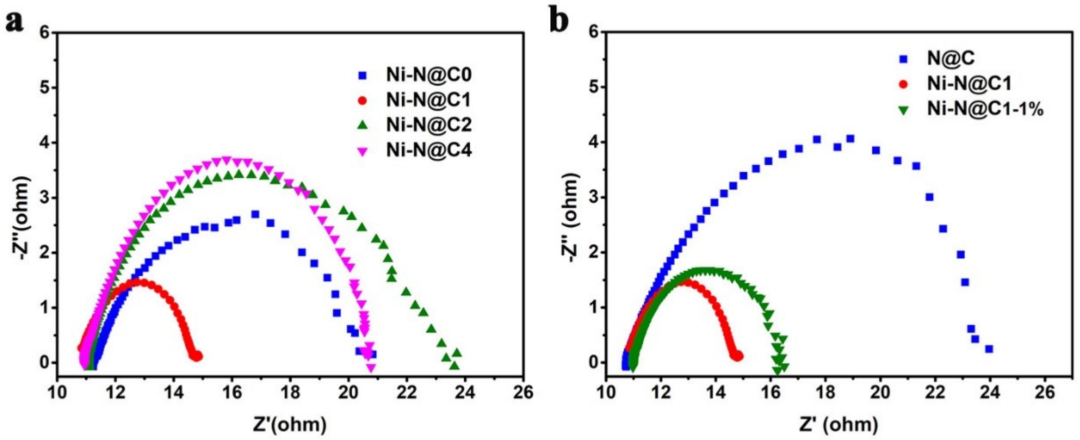

Figure S16. Nyquist plots of the catalysts.

The effect of pyrolysis temperature. Ni-PANI@C1 precursor was pyrolyzed at different carbonization temperature (800, 900 and 1000 °C) for 1 h with the heating rate of 5 °C/min under flowing N_2 atmosphere. After cooling down to room temperature, the samples were further stirred in 0.1 M HCl for 24 h to remove the residual salt and metal nanoparticles, then filtered, washed with deionized water, and dried under vacuum to afford Ni-N@C1-T (T=800, 900, 1000) materials. The ICP-OES analysis revealed that the contents of Ni are 0.533%, 0.514%, 0.237% for Ni-N@C1-800, Ni-N@C1-900, and Ni-N@C1-1000, respectively.

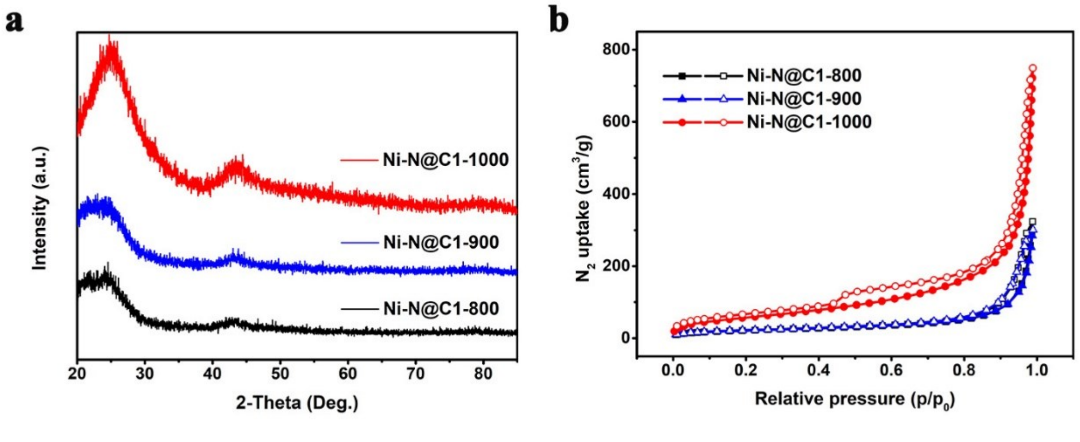

Figure S17. (a) XRD patterns and (b) N_2 adsorption and desorption isotherms of Ni-N@C1-T catalysts.

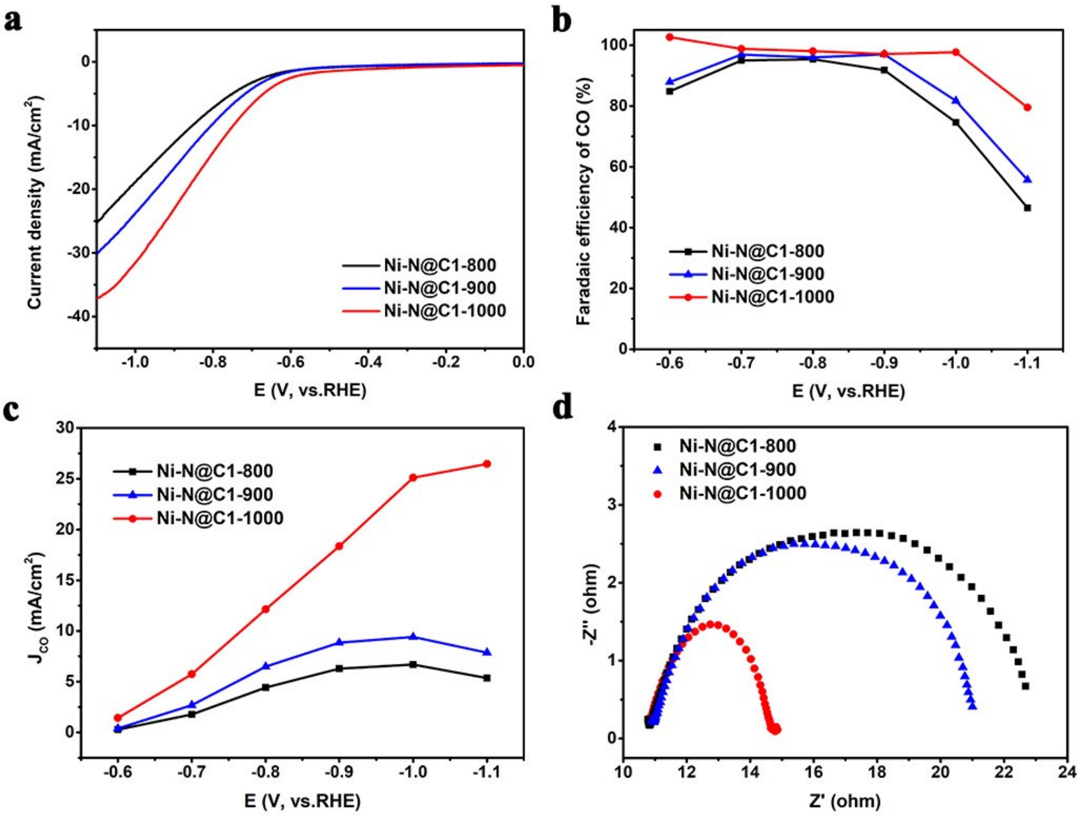

Figure S18. (a) Linear sweep voltammetric curves, (b) Faradaic efficiencies of CO, (c) Partial current density of CO, and (d) Nyquist plots of Ni-N@C1-T catalysts.

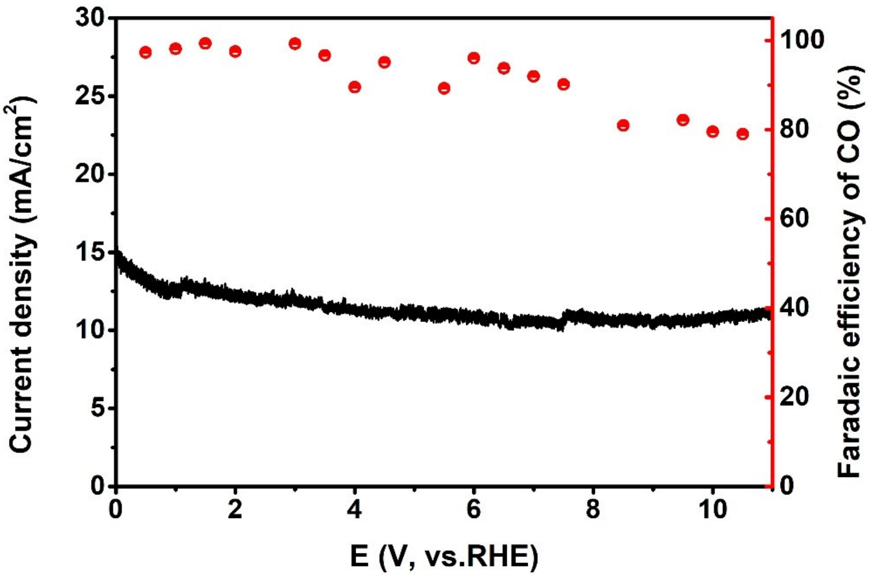

Figure S19. Stability of Ni-N@C1 at a potential of -0.9 V vs. RHE during 11 h.

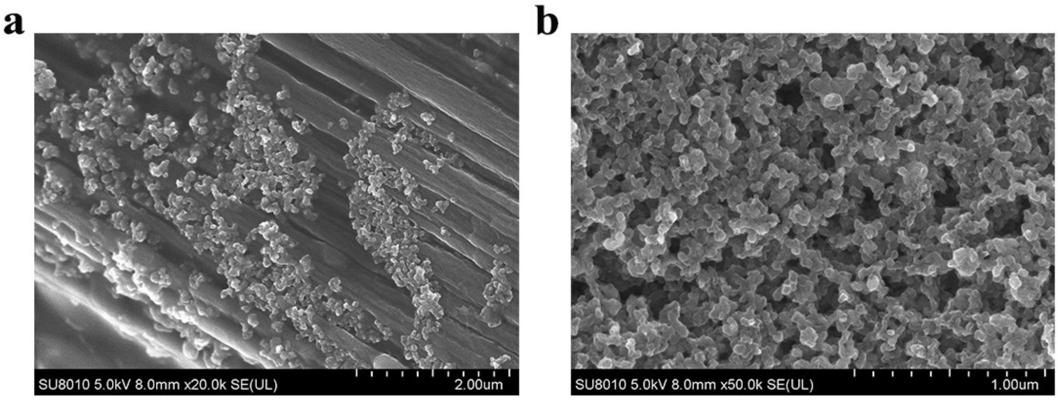

Figure S20. SEM images of Ni-N@C1-loaded electrode after CO_2RR test.

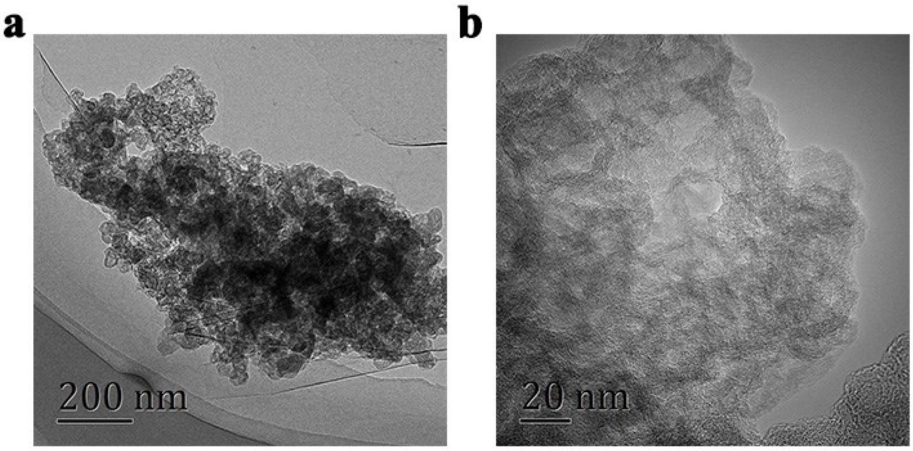

Figure S21. TEM images of Ni-N@C1 catalyst after CO_2RR test.

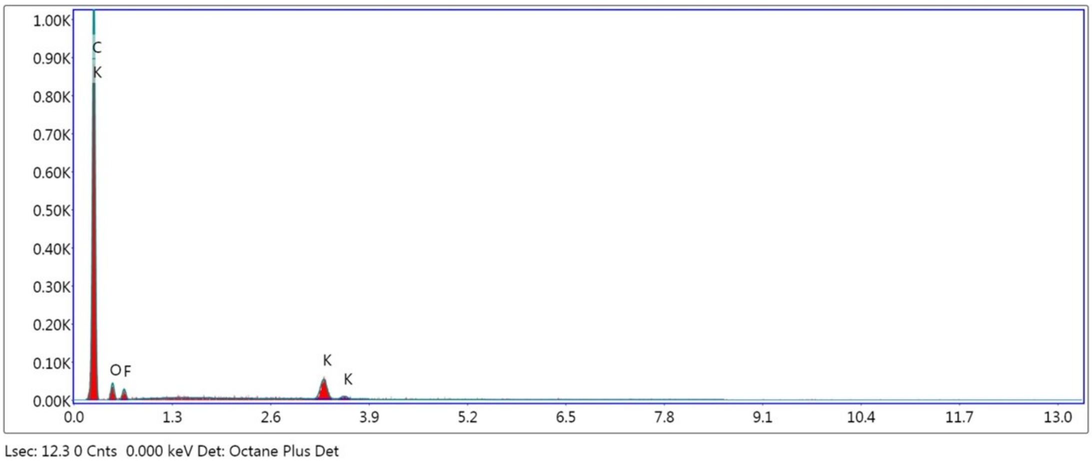

Figure S22. EDS result of Ni-N@C1 catalyst after CO_2RR test. (K and F come from $KHCO_3$ and Nafion, respectively)

3. Comparison of CO_2RR current densities and TOFs in reported single-atom Ni catalysts.

Table S5. Comparison of CO_2RR current densities and TOFs in reported single-atom Ni catalysts.

Sample (Ni wt%)	Electrolyte [a]	J_{CO} / $mA \cdot cm^{-2}$ (E vs. RHE)	TOF_{max}	J_{CO} / $A \cdot mg^{-1}$ Ni ($A \cdot mg^{-1}$ cat.)
Ni SAs/N-C[2] (1.53)	0.5 M $KHCO_3$ carbon paper	7.54 (-1.0 V)	5273 h^{-1}	4.8(0.073)
Ni–N–C[3] (1.25)	0.5 M $KHCO_3$ carbon paper	11.63 (-0.9 V)	~2037 h^{-1}	~1.86(0.023)
NiPor-CTF[4] (3.27)	0.5 M $KHCO_3$ carbon paper	51.3 (-0.9 V)	1701 h^{-1}	1.55(0.051)
Ni/N-PC[4] (1.50)	0.5 M $KHCO_3$ carbon paper	27.8 (-0.9 V)	2028 h^{-1}	1.85(0.028)
A-Ni-NSG[5] (2.8)	0.5 M $KHCO_3$ glassy carbon, RDE	35.4 (-0.72 V)	14800 h^{-1}	13.5(0.38)
$Ni-N_4-C$[6] (1.41)	0.5 M $KHCO_3$ glassy carbon	28.3 (-0.81 V)	~10782 h^{-1}	~9.85(0.14)
Ni–NG[7] (0.44)	0.5 M $KHCO_3$ glassy carbon; 0.1 M $KHCO_3$ GDE [b]	~7.5 (-0.86 V) 48.5 [b]	76320 h^{-1} 210000 h^{-1} [b]	69.7(0.31) 192(0.84)[b]
Ni-N-Gr[8] (2.2)	0.1 M $KHCO_3$ glassy carbon	~1.43 (-0.9 V)	7000 h^{-1}	6.4(0.14)
Ni-N-C[9] (0.24)	0.5 M $KHCO_3$ glassy carbon	3.63 (-0.67 V)	~3312 h^{-1}	~3.02(0.007)
Ni^{2+}@NG[10] (~0.8)	0.5 M $KHCO_3$ glassy carbon	9.38 (-0.68 V)	~4199 h^{-1}	~3.84(0.03)

Ni-N-C[11] (1.73)	0.1 M $KHCO_3$ -	~14 (-0.85 V)	27 mmol·h^{-1}·m^{-2}	16.5(0.29)
Ni–C–N[12] (1.63)	0.5 M $KHCO_3$ glassy carbon	10.4 (-0.8 V)	3079 h^{-1}	2.8(0.046)
Ni-N-MEGO[13] (6.9)	0.5 M $KHCO_3$ carbon paper	26.8 (-0.7 V)	864 s^{-1}	0.79(0.055)
Ni SAs/NCNTs[14] (6.63)	0.5 M $KHCO_3$ carbon cloth	54.2 (-1.0 V)	1176 h^{-1}	1.07(0.071)
NiN-GS[15] (~1[c])	0.1 M $KHCO_3$ glassy carbon	~4 (-0.82 V)	28800 h^{-1}	~26.3(0.02)
C-Zn_1Ni_4 ZIF-8[16] (5.44)	0.5 M $KHCO_3$ carbon paper	70.1 (-1.03 V)	10087 h^{-1}	9.2(0.50)
Ni–N–C[17] (0.16[c])	0.1 M $KHCO_3$ carbon paper	17.13 (-0.98 V)	-	- (0.029)
NiSAs/PTF[18] (1.11)	0.5 M $KHCO_3$ carbon paper	~37.5 (-1.2 V)	13462 h^{-1}	~14.1(0.16)
Ni-N@C1 (this work) (0.237)	0.5 M $KHCO_3$ carbon paper	26.5 (-1.1 V)	-	37.2(0.088)

[a] tested by three-electrode H-cell configuration unless noticed; [b] tested by anion membrane electrode assembly (MEA); [c] atom%.

References

1. B. Ravel and M. Newville, *J. Synchrotron Radiat.*, 2005, **12**, 537-541.
2. C. Zhao, X. Dai, T. Yao, W. Chen, X. Wang, J. Wang, J. Yang, S. Wei, Y. Wu and Y. Li, *J. Am. Chem. Soc.*, 2017, **139**, 8078-8081.
3. C. Z. Yuan, K. Liang, X. M. Xia, Z. K. Yang, Y. F. Jiang, T. Zhao, C. Lin, T. Y. Cheang, S. L. Zhong and A. W. Xu, *Catal. Sci. Technol.*, 2019, **9**, 3669-3674.
4. C. Lu, J. Yang, S. Wei, S. Bi, Y. Xia, M. Chen, Y. Hou, M. Qiu, C. Yuan, Y. Su, F. Zhang, H. Liang and X. Zhuang, *Adv. Funct. Mater.*, 2019, **29**, 1806884.
5. H. B. Yang, S. F. Hung, S. Liu, K. D. Yuan, S. Miao, L. P. Zhang, X. Huang, H. Y. Wang, W. Z. Cai, R. Chen, J. J. Gao, X. F. Yang, W. Chen, Y. Q. Huang, H. M. Chen, C. M. Li, T. Zhang and B. Liu, *Nature Energy*, 2018, **3**, 140-147.
6. X. Li, W. Bi, M. Chen, Y. Sun, H. Ju, W. Yan, J. Zhu, X. Wu, W. Chu, C. Wu and Y. Xie, *J. Am. Chem.*

Soc., 2017, **139**, 14889-14892.

7. K. Jiang, S. Siahrostami, T. Zheng, Y. Hu, S. Hwang, E. Stavitski, Y. Peng, J. Dynes, M. Gangisetty, D. Su, K. Attenkofer and H. Wang, *Energy Environ. Sci.*, 2018, **11**, 893-903.
8. P. Su, K. Iwase, S. Nakanishi, K. Hashimoto and K. Kamiya, *Small*, 2016, **12**, 6083-6089.
9. X. M. Hu, H. H. Hval, E. T. Bjerglund, K. J. Dalgaard, M. R. Madsen, M. M. Pohl, E. Welter, P. Lamagni, K. B. Buhl, M. Bremholm, M. Beller, S. U. Pedersen, T. Skrydstrup and K. Daasbjerg, *ACS Catal.*, 2018, **8**, 6255-6264.
10. W. Bi, X. Li, R. You, M. Chen, R. Yuan, W. Huang, X. Wu, W. Chu, C. Wu and Y. Xie, *Adv. Mater.*, 2018, **30**, e1706617.
11. W. Ju, A. Bagger, G. P. Hao, A. S. Varela, I. Sinev, V. Bon, B. Roldan Cuenya, S. Kaskel, J. Rossmeisl and P. Strasser, *Nat. Commun.*, 2017, **8**, 944.
12. Y. L. Zheng, J. Y. Han, L. Takele, F. Xie, Y. Zhang, J. Q. Sun, B. Han, J. Chen, Y. Gao and Z. Y. Tang, *Inorg. Chem. Front.*, 2019, **6**, 1729-1734.
13. Y. Cheng, S. Y. Zhao, H. B. Li, S. He, J. P. Veder, B. Johannessen, J. P. Xiao, S. F. Lu, J. Pan, M. F. Chisholm, S. Z. Yang, C. Liu, J. G. Chen and S. P. Jiang, *Appl. Catal. B-Environ.*, 2019, **243**, 294-303.
14. P. L. Lu, Y. J. Yang, J. N. Yao, M. Wang, S. Dipazir, M. L. Yuan, J. X. Zhang, X. Wang, Z. J. Xie and G. J. Zhang, *Appl. Catal. B-Environ.*, 2019, **241**, 113-119.
15. K. Jiang, S. Siahrostami, A. J. Akey, Y. Li, Z. Lu, J. Lattimer, Y. Hu, C. Stokes, M. Gangishetty, G. Chen, Y. Zhou, W. Hill, W.-B. Cai, D. Bell, K. Chan, J. K. Nørskov, Y. Cui and H. Wang, *Chem*, 2017, **3**, 950-960.
16. C. Yan, H. Li, Y. Ye, H. Wu, F. Cai, R. Si, J. Xiao, S. Miao, S. Xie, F. Yang, Y. Li, G. Wang and X. Bao, *Energy Environ. Sci.*, 2018, **11**, 1204-1210.
17. F. P. Pan, H. G. Zhang, Z. Y. Liu, D. Cullen, K. X. Liu, K. More, G. Wu, G. F. Wang and Y. Li, *J. Mater. Chem. A*, 2019, **7**, 26231-26237.
18. Y. Hou, Y.-B. Huang, Y.-L. Liang, G.-L. Chai, J.-D. Yi, T. Zhang, K.-T. Zang, J. Luo, R. Xu, H. Lin, S.-Y. Zhang, H.-M. Wang and R. Cao, *CCS Chemistry*, 2019, **1**, 384-395.